

Research Article

Multidisciplinary Optimization of Aerocapture Maneuvers

Roberto Armellin and Michèle Lavagna

Dipartimento di Ingegneria Aerospaziale, Politecnico di Milano, Via La Masa 34, 20156 Milano, Italy

Correspondence should be addressed to Roberto Armellin, armellin@aero.polimi.it

Received 15 July 2007; Accepted 13 December 2007

Recommended by Alex Freitas

A multidisciplinary-multiobjective optimization of aerocapture maneuvers is presented. The proposed approach allows a detailed analysis of the coupling among vehicle's shape, trajectory control, and thermal protection system design. A set of simplified models are developed to address this analysis and a multiobjective particle swarm optimizer is adopted to obtain the set of Pareto optimal solutions. In order to deal with an unconstrained multiobjective optimization, a two-point boundary value problem is formulated to implicitly satisfy the constraints on the atmospheric exit conditions. The trajectories of the most promising solutions are further optimized in a more refined dynamical system by solving an optimal control problem using a direct multiple shooting transcription method. Furthermore, a more complete vehicle control is considered. All the simulations presented consider an aerocapture at Mars with a polar orbit of 200 km of altitude as target orbit.

Copyright © 2008 R. Armellin and M. Lavagna. This is an open access article distributed under the Creative Commons Attribution License, which permits unrestricted use, distribution, and reproduction in any medium, provided the original work is properly cited.

1. INTRODUCTION

Aerocapture is a state-of-the-art technology considered to reduce the cost of planetary exploration. This technique, firstly proposed by Cruz in 1979 [1], allows the reduction of fuel cost for planetary insertion by using atmospheric drag to decrease the total orbital energy of the vehicle. The aerocapture is designed to aerodynamically decelerate a spacecraft from hyperbolic approach to a captured orbit within a single pass through the atmosphere with no propulsion exploitation. Once the vehicle enters the atmosphere, bank angle modulation is used to safely remain within the flight corridor, preventing skip-out or planetary impact. Propulsion is used for attitude control and periapsis raise only.

Several missions—such as Magellan and Mars Global Surveyor—have already employed aerobraking strategy: multiple atmospheric passes over an extended period of time allow to gradually get the desired orbit; but in these cases an impulsive maneuver is first required to make the target planet capture the spacecraft. Future missions, like either robotic and human missions to Mars or the Titan Explorer, are considering using a lifting body to perform an aerocapture maneuver at the arrival planet: a lifting body is less sensitive to variation in the entry angle and the drag is easily modulated. As counterpart, sophisticated guidance algorithms are

required to successfully drive the vehicle in the atmospheric path.

Many studies in the last thirty years focused on the aerocapture maneuver optimization. This optimization was mainly conducted in terms of trajectory: the shape and the aerodynamic characteristics were fixed. Within this framework many techniques were developed to optimize an aerocapture maneuver focusing on different control variables and on the minimization of the path constraints [2–6].

Bearing in mind space utilization and exploration, the payload mass delivery's capability is an open issue that leads to a wider analysis of aeroassisted maneuvers. The shape definition could be considered as an additional degree of freedom to enhance the overall maneuver efficiency. In this frame, parametric studies analyzing the influence of different shapes on the considered maneuvers were accomplished [7, 8].

The influence of variation of shape on this class of problems shows the high sensitivity the aeroassisted maneuvers have, and confirms the need of a multidisciplinary approach. In this context, the work of Sudmeijer and Mooij underlined the relevance of the shape optimization process to improve the performance of reentry probes [9].

A multidisciplinary-multiobjective approach for the coupled vehicle's shape and trajectory optimization of aerogravity assist maneuvers has been recently proposed by the

authors [10]. The coupling among vehicle's shape, trajectory control, and heating rates has been exploited and a tool useful for the preliminary design of aerogravity assist maneuvers has been developed.

A similar architecture is here proposed to address the preliminary design of aerocapture maneuvers from a multidisciplinary-multiobjective standpoint. It is important to note that the aerocapture modeling and the optimization problem setup is completely different from the aerogravity assist one. In fact, a capsule-like vehicle is considered, a different control strategy is employed (exploiting both the angle of attack and the bank angle), and a different set of ordinary differential equations is carried out for the simplified dynamical model. Furthermore, the optimization process is aimed in this case to minimize the thermal protection system mass and to maximize the volumetric efficiency of the capsule, thus optimizing the payload mass delivery capability. Moreover, the aerocapture optimization problem is more challenging, as it involves the solution of a boundary value problem within each objective function evaluation. This expedient is necessary both to avoid equality constraints and to bound the propellant required for the periapsis raise.

A multiobjective particle swarm optimizer (MOPSO) is applied to detect the set of Pareto optimal solutions of the analyzed problem. The particle swarm optimization (PSO) method has been introduced for the first time by Kennedy and Eberhart in 1995 [11, 12]. Since its introduction several works have been carried out on PSO improving the original method and proving its efficiency; an overview of the more important ones is given by Poli et al. in [13]. In recent years there have been several proposals to extend particle swarm optimization to multiobjective optimization problems [14–18]. The algorithm implemented in this work is based on that proposed by Coello et al., the adoption of a variable inertia and the application of the preservation of feasible solution method (FSM) being the two main differences.

The paper is organized as follows. The models developed for the multidisciplinary treatment of the maneuver are presented first. In particular the configuration, the aerodynamics, the thermal protection system (TPS), and the dynamics models are described. Some considerations on the clashing requirements of maximizing the vehicle volumetric efficiency and reducing the TPS mass follow. Subsequently the guidelines of the MOPSO implementations are given. The coupled vehicle's shape and trajectory optimization is then presented and results are discussed. As a conclusion the trajectory refinement is analyzed.

2. MODELS

2.1. Capsule

The capsules considered in this work are axisymmetric vehicles whose geometry is described by means of five parameters (r_n , r_b , r_r , θ , δ). These parameters are the vehicle nose radius, the base radius, the rear-base radius, the front cone half-angle, and the rear-cone half-angle, as shown in Figure 1.

By allowing a quite wide search space for the parameters, significantly different configurations can be obtained, from

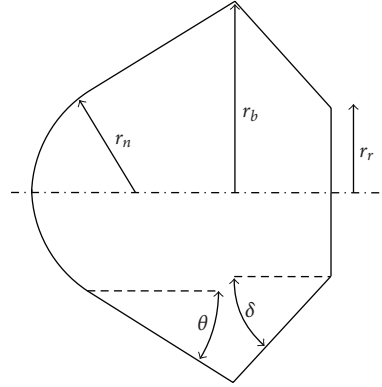


FIGURE 1: Shape parameters (r_n , r_b , r_r , θ , δ) visualization.

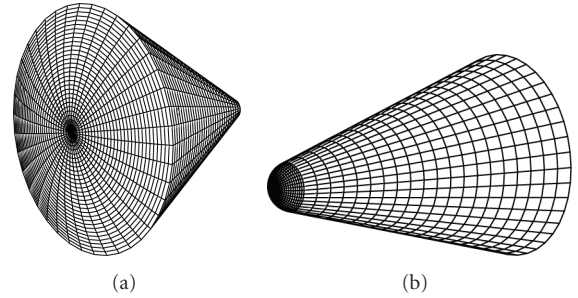


FIGURE 2: (a) Highly blunted vehicle and (b) slender vehicle.

highly blunted to slender vehicles, as reported in Figure 2. The base area $S = \pi r_b^2$ is considered as reference surface for aerodynamic coefficients. A constraint of 5 m^3 on capsule volume is considered. A density value $\rho_v = 230 \text{ kg/m}^3$ is considered for a volume of 3.8 m^3 , equivalent to that of Mars Express mission, whereas a reduced density value is considered for the exceeding volume, as it serves only as structural mass.

2.2. Newtonian flow

The aerodynamic properties for the capsule-like vehicles described in the previous section are computed by summing up the contributes given by each panel in which the geometry is discretized. The Newtonian flow theory with Lee modification is applied for the estimate of the pressure coefficient, C_p [19].

The modified Newtonian flow is a local surface inclination method in which C_p depends only on the local surface deflection angle α ; it does not depend on any surrounding flowfield. Within this approximation, the classical expression for the pressure coefficient can be derived as

$$C_p = C_{p_{\max}} \sin^2 \alpha, \quad (1)$$

where the maximum value of the pressure coefficients, $C_{p_{\max}}$, is evaluated at the stagnation point behind a normal shock wave by

$$C_{p_{\max}} = \frac{p_0 - p}{(1/2)\rho v^2}. \quad (2)$$

In the former expression p , v , and ρ are the asymptotic flow pressure, velocity, and density, respectively; p_0 indicates the stagnation point pressure. As the free stream collides only against the frontal area of a body and it cannot curl around the body and collide against the back surface, the shadow part of the body is characterized by free-stream pressure and therefore $C_p = 0$.

In order to encompass high temperature effects, the value of p_0 is computed with the NASA Chemical Equilibrium with Application code [20]. As a result the computed stagnation pressure takes into account of the high temperature effects that characterize hypersonic flows.

The aerodynamic code has been validated on the Viking lander capsule hypersonic aerodynamics data from on-ground and on-board measurements, which have been recently used by Edquist for comparison to the LAURA Navier-Stokes code [21]. A high accuracy, average errors lower than 6%, is achieved for both drag and lift-to-drag coefficients. The obtained accuracy is remarkably high and comparable to that attained through the sophisticated CFD code LAURA.

2.3. Thermal protection system

As aerodynamic efficiency is not a major issue for aerocapture application, and the heating rate experienced are comparable to previous Mars missions, ablative thermal protection systems are the natural selection for this kind of maneuvers. In fact, ablative materials can accommodate heating rates and heat loads through phase change and mass loss; this represents the classical approach to TPS used for over 40 years in a broad range of applications, and all NASA planetary entry probes (to date) have used it [22].

Therefore, the main issue for the aerocapture maneuver stays in lowering the TPS mass fraction. In fact the mass saving gained by reducing the propellant required for the achievement of the final orbit must not be jeopardized by the need of a heavy heat shield. An analysis on past NASA missions reveals a direct connection between the TPS mass fraction and the total heat q_0 experienced by the vehicles at the stagnation point. Based on this consideration, the TPS mass fraction is simply estimated through the power law fit curve:

$$\text{TPS \%} = \frac{m_{\text{TPS}}}{m} = 0.0091q_0^{0.51575}. \quad (3)$$

Neglecting the radiative heating, the total heat is calculated integrating the well-known relation for convective heating [23]:

$$\dot{q}_0 = 1.35(10^{-8}) \left(\frac{\rho}{r_n}\right)^{1/2} v^{3.04} \left(1 - \frac{h_w}{h_0}\right), \quad (4)$$

in which h_w is the wall enthalpy, and h_0 is the total enthalpy.

2.4. Dynamics

Two different sets of ordinary differential equations are chosen to describe the vehicle dynamics: a simpler formulation to facilitate the solution of the coupled trajectory and vehicle's shape optimization problem, and a more complex set for trajectory further refinement.

The complete dynamical model, written in a local noninertial reference frame, reads

$$\begin{aligned} \dot{r} &= v \sin \gamma, \\ \dot{\vartheta} &= \frac{v \cos \gamma \cos \psi}{r \cos \varphi}, \\ \dot{\varphi} &= \frac{v \cos \gamma \sin \psi}{r}, \\ \dot{v} &= \frac{D}{m} - g \sin \gamma, \\ v\dot{\gamma} &= \frac{L \cos \sigma}{m} - g \cos \gamma + \frac{v^2 \cos \gamma}{r}, \\ v\dot{\psi} &= \frac{L \sin \sigma}{m \cos \gamma} - \frac{v^2 \tan \varphi \cos \gamma \cos \psi}{r}, \end{aligned} \quad (5)$$

in which the state vector $(r, \vartheta, \varphi, v, \gamma, \psi)$ is made up by the orbital radius, the longitude, the latitude, the velocity, the flight path angle, and the heading angle of the spacecraft. Furthermore, $L = (1/2)\rho S C_L v^2$ and $D = (1/2)\rho S C_D v^2$ are the classical expressions for the lift and the drag force, σ is the bank angle and g the gravitational acceleration. (Consult [10] for a complete description of the dynamics.)

In the first phase of the optimization process, when the coupled shape and trajectory's optimization are considered, we are only concerned with parameters directly related to enter a closed orbit, no matter whether a specific three dimensional orbit the spacecraft will be finally placed on. For this reason, the variables of interest are r and v only. In order to analyze the behavior of these variables, the equation of flight path angle must also be taken into account. The simplified model for the aerocapture maneuver is made up by a set of three differential equations. To facilitate the analysis, the equations of motion are nondimensionalized [4]. The dimensionless arc length s replaces the time t :

$$ds = \sqrt{\frac{\beta}{r_e}} v dt. \quad (6)$$

The altitude is nondimensionalized with

$$y = \frac{\rho}{\rho_e} = e^{-\beta h}, \quad (7)$$

in which the altitude h is relative to the planet's atmosphere boundary, $h < 0$ means the vehicle is within the atmosphere. Note that a simple exponential model for the planetary density $\rho = e^{-\beta h}$ is considered, in which β is the inverse scale height of the atmosphere, whose boundary is fixed for Mars at 100 km of altitude. With the concerned speed, the following expression is used:

$$x = \ln \left(\frac{v_e}{v} \right)^2. \quad (8)$$

In the previous equations, and throughout the paper, the e subscript refers to properties at the atmosphere's boundary. The remaining required nondimensional parameters are defined by

$$\begin{aligned}\varepsilon &= \sqrt{\frac{\beta}{r_e} \frac{\rho_e S C_D}{m}}, \\ \delta &= \frac{\mu/r_e}{v_e^2},\end{aligned}\quad (9)$$

in which μ is the gravitational parameter of the planet. The complete nondimensional set of equations is then

$$\begin{aligned}\dot{y} &= -\sqrt{\beta r_e} y \sin \gamma, \\ \dot{x} &= \varepsilon y + \frac{2\delta e^x}{\sqrt{\beta r_e}} \sin \gamma, \\ \dot{\gamma} &= \frac{\varepsilon}{2} \left(\frac{C_L}{C_D} \right) \cos \sigma + \frac{\cos \gamma}{\sqrt{\beta r_e}} (1 - \delta e^x).\end{aligned}\quad (10)$$

The initial values of x and y are known from the entry condition in the planetary sphere of influence, whereas the entire final state is univocally defined if the apogee of the exit trajectory is prescribed to minimize the required Δv for the circularization. In order to have the same number of differential equations and boundary conditions, two differential equations must be added to the system (10). For this purpose, the arc length is scaled as $s = T\tau$ where τ belongs to the interval $[0, 1]$, and T is the unknown final arc length, which is an unknown constant. One additional differential equation is then $\dot{T} = 0$. Furthermore, if a constant bank angle control law is considered, the differential equation $\dot{\sigma} = 0$ can be used to match the number of equations and the number of boundary conditions. The constant bank angle approximation represents the simplest control law that can be adopted as far as the achievement of the tridimensional final orbit is not of concern. In this work frame, the complete set of equations in the new independent variable τ is

$$\begin{aligned}\dot{y} &= T \left(-\sqrt{\beta r_e} y \sin \gamma \right), \\ \dot{x} &= T \left(\varepsilon y + \frac{2\delta e^x}{\sqrt{\beta r_e}} \sin \gamma \right), \\ \dot{\gamma} &= T \left(\frac{\varepsilon}{2} \frac{C_L}{C_D} \cos \sigma + \frac{\cos \gamma}{\sqrt{\beta r_e}} (1 - \delta e^x) \right), \\ \dot{T} &= 0, \\ \dot{\sigma} &= 0.\end{aligned}\quad (11)$$

This set of equations is suitable to define the two-point boundary value problem (TPBVP) described in detail in the following section.

3. VOLUMETRIC EFFICIENCY AND TPS MASS PERCENTAGE ANALYSIS

To better understand the results of the following section, the effects of the vehicle's shape on the trajectory minimum altitude, on the heat shield percentage, and on the volumetric efficiency are analyzed firstly. The simplified model of the dynamic (11) is considered.

The selected control law imposes both bank angle σ and the angle of attack α to be constant; the C_L/C_D is, therefore, determined by the angle of attack α . The goal is to use the atmospheric path to reduce the Δv required to achieve a circular target orbit of 200 km of altitude. Within this frame, the atmospheric path is used to model the incoming hyperbola into an elliptical trajectory having the apogee at an altitude of 200 km, without considering the achievement of the 3D target orbit. The achieved orbital plane as the vehicle leaves the atmosphere, is assumed to be the target orbit plane: that matching condition is assured by a proper choice of the entry plane in the planet's atmosphere (i.e., the proper selection of the pericenter radius of the incoming hyperbola). The satisfaction of this constraint is addressed within the solution refinement process. The atmospheric path is computed by solving the TPBVP after the vehicle aerodynamic coefficients, the volume, and the mass have been computed. Some details of the TPBVP formulation are now illustrated.

The conditions at the edge of the atmosphere are labeled with the subscript e , those at Mars sphere of influence by ∞ , and the entry and exit conditions with the superscripts $-$ and $+$, respectively. The atmospheric boundary is settled at 100 km over Mars mean radius. The 2-body problem and (11) completely describes the system dynamics outside and inside the atmosphere respectively [24]. The velocity magnitude at the boundary of the sphere of influence is assigned to $v_\infty^- = 5$ km/s. At the atmospheric entry, the initial radius r_e^- is r_e and the entry velocity v_e^- is computed by the solution of the Vis-Viva equation:

$$\frac{1}{2} v_e^{-2} - \frac{\mu}{r_e} = \frac{1}{2} v_\infty^{-2}. \quad (12)$$

In order to apply a tangential Δv correction, which represents the minimum propellant strategy, the apogee r_a of the trajectory obtained after the atmospheric phase is constrained to lie on the target orbit. Thus, the values of γ_e^+ and Δv required for the circularization can be computed as a function of the final velocity v_e^+ through the following procedure.

- (1) Evaluate the energy of the exit trajectory:

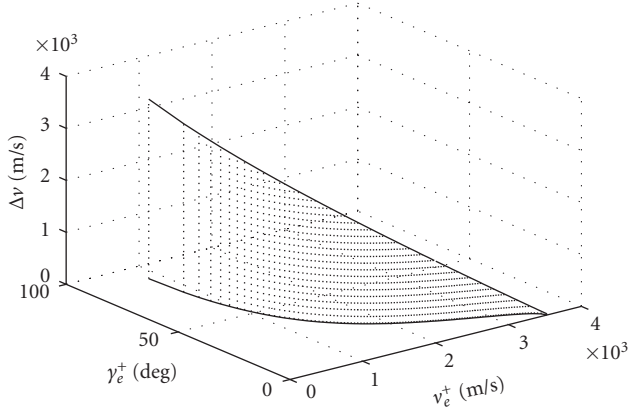
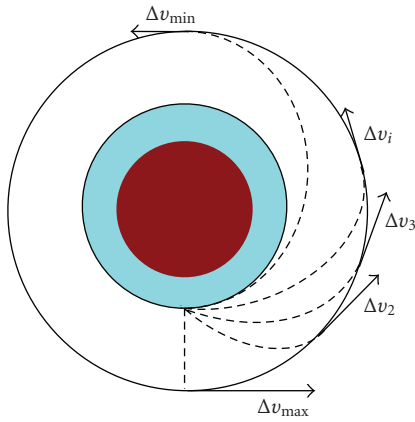
$$E = \frac{1}{2} v_e^{+2} - \frac{\mu}{r_e^+}. \quad (13)$$

- (2) Compute the semimajor axis and the eccentricity:

$$\begin{aligned}a &= -\frac{\mu}{2E}, \\ e &= \frac{r_a}{a} - 1.\end{aligned}\quad (14)$$

- (3) Obtain the angular momentum:

$$\Gamma = \sqrt{a(1 - e^2)}\mu. \quad (15)$$

FIGURE 3: The v_e^+ - γ_e^+ constraint and the associated Δv .FIGURE 4: Sketch of the periaresis raise Δv .

- (4) Finally, compute the exit flight path angle and the Δv burn:

$$\gamma_e^+ = \arccos\left(\frac{\Gamma}{v_e^+ r_e^+}\right), \quad (16)$$

$$\Delta v = \sqrt{\frac{\mu}{r_a}} - \sqrt{-\frac{\mu}{a} + 2\frac{\mu}{r_a}}.$$

The procedure admits solutions of Figure 3 for values of v_e^+ in the range [825.9, 3527.4] m/s.

A subset of exit trajectories with the apogee on the target orbit are sketched in Figure 4. The Δv_{\max} corresponds to the unrealistic vertical exit from the atmosphere. In that case the spacecraft would arrive at the apogee at zero velocity, resulting in a $\Delta v = 3453.7$ m/s: the circular target orbit velocity. The minimum Δv correction is 24.4 m/s and it is associated to the maximum exit velocity $v_e^+ = 3527.4$ m/s and to the minimum exit flight path angle $\gamma_e^+ = 0$ deg. The exit trajectory can be identified with an Hohmann transfer connecting the circular orbit at the atmosphere boundary to the target orbit, with the main difference being only the apogee impulse to be required.

To facilitate the TPBVP numerical solution, a 3500 m/s constraint on v_e^+ is posed; the resultant γ_e^+ and Δv are 1.73 deg

and 52.6 m/s, respectively. It's worth noting that the computed trajectories are not optimal from the Δv standpoint, although the selected constraints assure them to be close to the theoretical minimum (considering the required additional propellant). The proposed procedure assures a complete knowledge of the final state x , y , and γ ; the remaining unknowns, that is, the total arc length T , the entry flight path angle γ_e^- and the bank angle σ , are computed by the TPBVP solver. A linear multipoint method [25–27] is applied to solve the problem and the second order solution derived by Vihn et al. [4] is used as first guess solution. The algorithm shows quadratic convergence typical of Newton's method and converges on average within 10 iterations. The integration interval is transcribed using 100 nodes to assure absolute and relative accuracy of 10^{-8} .

The Δv correction is univocally determined once the constraints on the final conditions are satisfied, therefore no Δv optimization is required. As the Δv minimization is substituted by a constraint satisfaction problem, the attention can be focused on two other important aspects of the aerocapture design: the vehicle volumetric efficiency maximization and the TPS mass fraction minimization. A high volumetric efficiency has two main benefits: a smaller launcher fairing is required as the vehicle is more bulky, and the vehicle's volume can be better exploited for the spacecraft accommodation. The minimization of the TPS mass ratio leads to a maximization of the mission outcome, as the percentage of payload mass increases. It needs to be remarked that the TPS mass must be lower than the propellant required to achieve the target trajectory without using the aerocapture in order to consider the aerocapture beneficial. These goals are monitored by the TPS mass fraction of (3) and

$$\eta = \frac{l_{\max}}{V}, \quad (17)$$

where l_{\max} is the maximum linear dimension of the capsule. The main difference between these two indexes is that η is simply a geometric value, whereas TPS% depends on the vehicle's geometry and on the atmospheric trajectory.

It is now shown that these indexes have clashing behaviors, thus justifying the multiobjective optimization approach described in the following section. The vehicles of Figures 5 and 6 are considered to clarify this concept: the first one is more compact and it is characterized by $\eta = 0.59 \text{ m}^{-2}$, the second has a bigger base area and being shorter, resulting in $\eta = 0.71 \text{ m}^{-2}$. Both the shapes have a volume of 5 m^3 , and the same trim angle of attack $\alpha = -20$ deg. The bank angle that guarantees the satisfaction of the constraint on the exit conditions is $\sigma = 163.05$ deg for the first shape and $\sigma = 115.7$ deg for the second. Figures 7 and 8 describe the atmospheric path and the velocity history. Shape 1 requires a steeper entry, a longer maneuver, and a lower altitude in order to achieve the required kinetic energy loss. As a result, the vehicle experiences a greater value of total heat load, therefore a greater TPS mass is needed. More specifically, the TPS mass percentage are 9.48 and 7.44 for Shape 1 and Shape 2, respectively. In general, for a given mass, a more compact vehicle (i.e., high volumetric efficiency) must fly deeper into the atmosphere to lose its kinetic energy, thus experiencing

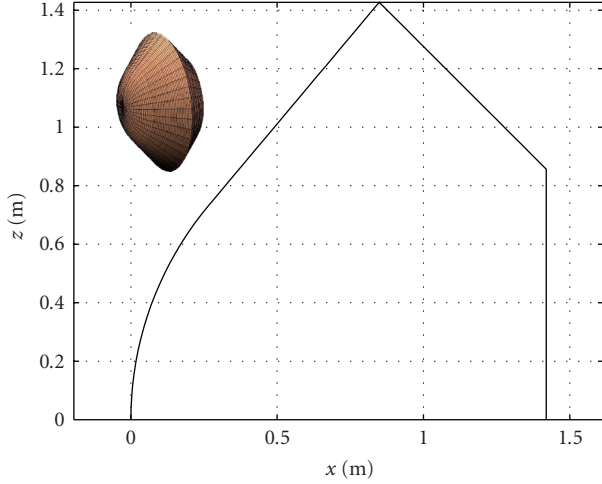


FIGURE 5: Shape 1, volumetric efficiency oriented vehicle.

high thermal loads (i.e., high TPS mass). It should be underlined that within the framework of constant vehicle volume and density, the performance index η plays a role similar to that of the ballistic coefficient, defined as $m/(SC_D)$, and frequently used in literature. A high volumetric efficiency translates into a high ballistic coefficient (see Table 1), thus a great value of atmosphere density is required to produce a significant amount of drag. Furthermore, for a fixed shape, the ballistic coefficient almost linearly increases with the vehicle's dimension. That is the reason why special devices like parachutes or ballutes are considered when the aerocapture maneuver for human missions to Mars is studied.

4. MULTIDISCIPLINARY OPTIMIZATION

4.1. Multiobjective particle swarm optimizer

As shown in the previous section, it is difficult to identify a single objective function when designing an aerocapture maneuver. In order to use classic optimization codes (i.e., gradient based methods) to solve a multiobjective optimization problem a common practise is to merge the different objective functions into a single scalar objective function by means of weighting factors. This technique requires an accurate selection of the weights, and it has, as major drawback, the identification of a single optimal solution per run. On the contrary, population-based optimizers can be more easily modified to deal with a vector of objective functions delivering the entire set of Pareto optimal solutions. Furthermore, particle swarm optimization seems particularly suitable for multiobjective optimization mainly because of the high speed of convergence that the algorithm presents for single-objective optimization [28]. In a multiobjective optimization problem, the objective function is an M -dimensional vector:

$$\mathbf{f}(\mathbf{x}) = (f_1(\mathbf{x}), f_2(\mathbf{x}), \dots, f_M(\mathbf{x})). \quad (18)$$

In this frame, a criterion to compare vectors is necessary to identify the optimal solution set. The Pareto dominance is

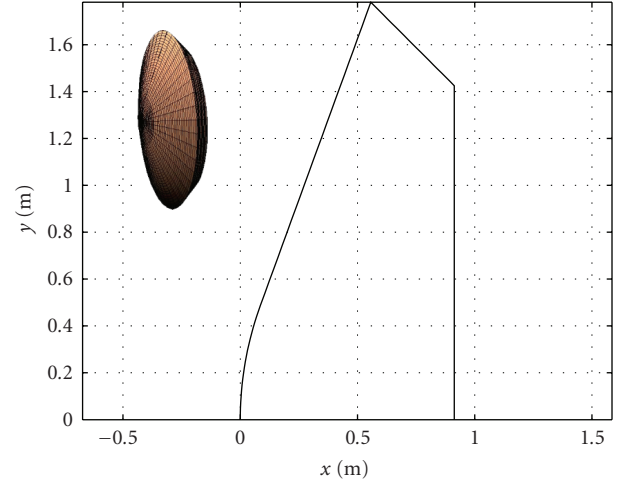


FIGURE 6: Shape 2, TPS% oriented vehicle.

the appropriate criterion to serve this aim, enabling the solutions ranking [29].

The MOPSO implemented for the solution of the problem at hand is based on the following algorithmic flow.

- (1) Randomly initialize a number of individuals or particles N within the design space.
- (2) Evaluate the objective function:

$$\mathbf{y}_i = \mathbf{f}(\mathbf{x}_i) \quad \text{for } i = 1, \dots, N. \quad (19)$$

- (3) Update the personal best solution \mathbf{p}_{best} . The solutions are compared using the Pareto dominance criterion. Thus, for each particle we have

$$\mathbf{p}_{\text{best}} = \begin{cases} \mathbf{x}_i, & \text{if } \mathbf{x}_i \text{ dominates } \mathbf{p}_{\text{best}}, \\ \mathbf{p}_{\text{best}}, & \text{if } \mathbf{p}_{\text{best}} \text{ dominates } \mathbf{x}_i, \\ \mathbf{x}_i \text{ or } \mathbf{p}_{\text{best}}, & \text{randomly in the other cases.} \end{cases} \quad (20)$$

$$\text{for } i = 1, \dots, N,$$

- (4) Update global best list \mathbf{G}_{best} . In the multiobjective problem, \mathbf{G}_{best} is the analogous of the scalar global best \mathbf{g}_{best} and it represents the entire set of nondominated solutions. This list is updated by processing the subset of nondominated solutions \mathbf{x}_j with $j = 1, \dots, N^* \leq N$.
 - (i) If \mathbf{x}_j is dominated by one of the solution belonging to the list, do not updated the list.
 - (ii) If \mathbf{x}_j dominates one or more solutions belonging to the list, then add \mathbf{x}_j to the \mathbf{G}_{best} list and delete the dominated solutions.
 - (iii) If \mathbf{x}_j neither dominates nor is dominated by any solution belonging to the \mathbf{G}_{best} list, then simply add \mathbf{x}_j to the list.
- (5) Update the global best solution \mathbf{g}_{best} . Note that the \mathbf{g}_{best} is univocally defined for a scalar objective function, whereas it must be opportunely chosen within

TABLE 1: Numerical results for the two analyzed shapes.

Parameter		Shape 1	Shape 2
TPS%	—	9.48	7.44
η	m^{-2}	0.56	0.71
α	deg	-20	-20
σ	deg	163.18	115.7
C_L/C_D	—	0.15	0.31
$m_0/(SC_D)$	kg/m^2	135.99	69.62
h_{\min}	km	43.01	48.6
γ_{ε}^-	deg	-8.57	-8.11

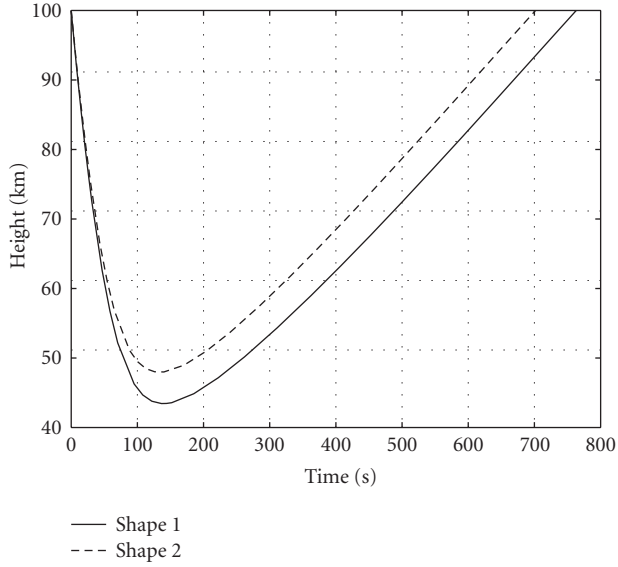


FIGURE 7: Shape 1 and Shape 2 altitude profile comparison.

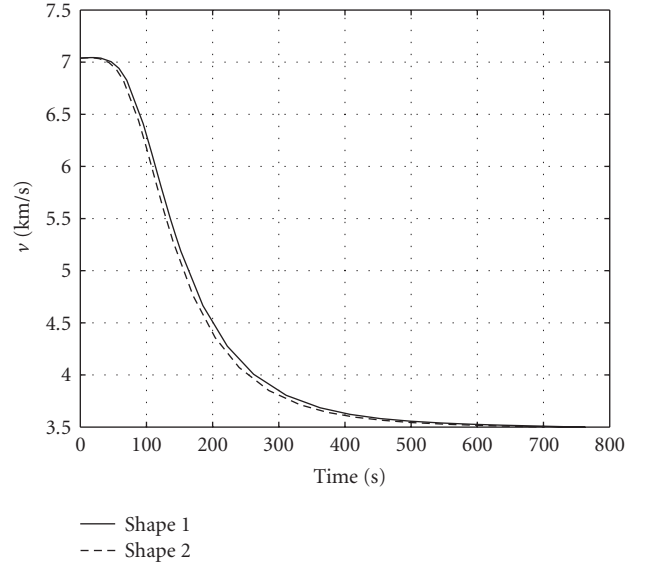


FIGURE 8: Shape 1 and Shape 2 velocity comparison.

the \mathbf{G}_{best} list in the multiobjective case. The selection of the \mathbf{g}_{best} plays a key role in obtaining a uniform set of Pareto optimal solutions. For this purpose, a uniform 30-cell grid in the objective space is defined at each iteration and the number of solutions belonging to each grid cell is calculated. Based on this number, a roulette-wheel method is then applied to promote the selection of \mathbf{g}_{best} in a low-populated grid cell.

- (6) Compute the new particles position by

$$\mathbf{x}_i^{k+1} = \mathbf{x}_i^k + \mathbf{v}_i^{k+1} \Delta t \quad \text{for } i = 1, \dots, N, \quad (21)$$

in which \mathbf{v}_i^{k+1} is the velocity of the i th particle at the $(k+1)$ iteration, given by

$$\mathbf{v}_i^{k+1} = w \mathbf{v}_i^k + c_1 r_1 \frac{\mathbf{x}_i^k - \mathbf{p}_{\text{best}}}{\Delta t} + c_2 r_2 \frac{\mathbf{x}_i^k - \mathbf{g}_{\text{best}}}{\Delta t}. \quad (22)$$

- (7) Repeat (2)–(6) until the convergence criterion is satisfied or the maximum number of iterations is reached.

The parameters c_1 and c_2 of (22) are considered constant and equal to 2 during the optimization, assuring a balance

between local and global terms. A linear decrease of w with the iteration number in the interval $[0.4, 1.4]$ is adopted. In particular a greater value of the inertia enables a better exploration of the search domain in the first phase of the optimization, whereas a lower value allows a better analysis of the most promising areas of research space in the subsequent phases. Note that if the position of a particle goes outside the search space, the violated component of the decision vector takes the value of the corresponding boundary and its velocity component is multiplied by a random number between $[-1, 0]$.

The maximum numbers of particle belonging to the \mathbf{G}_{best} is fixed to 100 units. The same procedure adopted for selecting the \mathbf{g}_{best} is used to delete those solutions belonging to a highly populated grid-cell, if the maximum list size is exceeded.

The problem addressed with implemented MOPSO is characterized by the presence of inequality constraints necessary to guarantee a minimum aerodynamic performance and vehicle's length. As the feasible domain inside the search space is sufficiently large the FSM is adopted for the constraints handling [30]. More specifically the swarm

initialization is performed randomly, but only feasible solutions are retained. This implies that the first step of the algorithm generally requires the evaluation of a number of solutions greater than the population size. Furthermore, only feasible solutions are counted for the \mathbf{g}_{best} and \mathbf{p}_{best} values during the optimization. The initial velocity of the particle is set to be 0.

The convergence criterion adopted is based on the comparison of the average position of the non dominated solutions in the objective space with the same average position of the previous 20 iterations. If the componentwise difference of this two vectors is lower than 1% the Pareto set of optimal solutions is assumed to have been found. Furthermore, a maximum number of iterations of 100 and a 20-particle swarm are considered. These values are chosen, on the basis of several experiments, to assure an acceptable repeatability of the Pareto optimal solution set with a limited computational time.

4.2. Optimization architecture

Since the minimization of η and TPS% are two clashing requirements, a multiobjective optimization architecture is adopted. The overall optimization architecture is then given, the scheme of Figure 9 can be used as a visual aid. The optimization variables are the four geometric parameters $r_n \in [0.1, 0.9]$, $r_r \in [0.2, 0.9]$, $\theta \in [20, 70]$ deg, $\delta \in [5, 60]$ deg, and the angle of attack $\alpha \in [-30, 30]$ deg. Note that the vehicle nose radius and the rear radius are expressed as fraction of the base radius, whose value is computed to satisfy the constraint of 5 m^3 for the capsule's volume. The sphere of influence entry velocity $v_\infty = 5 \text{ km/s}$ and the vehicle's density $\rho_v = 230 \text{ kg/m}^3$ are user provided constants necessary to define the optimization problem.

For each set of optimization variables the vehicle's aerodynamic performance at the trim angle of attack are computed. At this point the TPBVP can be formulated and solved, delivering the total heat load experienced by the vehicle. The γ_e^+ is constrained to 1.73 deg as in Section 3, resulting in the same Δv of 52.6 m/s for all the solutions. The two performance indexes are then simply evaluated and the optimizer iterates until the convergence criterion is satisfied or the maximum iteration number reached. Two simple inequality constraints are also considered on the lift-to-drag ratio, $|L/D| \geq 0.3$, and vehicle length, $l \geq 0.8 \text{ m}$. The first one is necessary to provide the vehicle with a means to accurately control the atmospheric path, the second removes solutions with extremely short length from the search space. A function evaluation takes on average 1.26 s on a Intel Pentium 4, 2.53 GHz Desktop.

4.3. Experiments and results

The values of the MOPSO parameters given in Section 4.1 are the result of a tuning process based on several experiments in which the swarm size, the maximum number of iterations, and the value of the inertia have been changed. The average behavior of the algorithm is shown in Figure 10 with a plot of 30 simulations in which the solutions belong-

ing to the \mathbf{G}_{best} list are interpolated by means of cubic splines to avoid cluttering the plot. The result is satisfactory from the preliminary design point of view. The algorithm is very effective in computing the Pareto optimal solutions for low TPS mass vehicles; on the other hand suboptimal solutions appear in the high volumetric efficiency region. This behavior is mainly due to the difficulty in finding feasible solutions of the TPBVP when compact capsules are considered. In these cases, is not always possible to decelerate the vehicle's as required to satisfy the constraints imposed in the TPBVP formulation. Furthermore, note that the poor behavior in the flat part of the Pareto front is due more to the interpolation process than to the actual values of the solutions. Only 5 simulations out of 30 stop for the satisfaction of the convergence criteria, whereas the remaining ones reach the maximum number of iterations. Nevertheless, it has been noticed that increasing the iterations does not significantly improve the quality of the solution, whereas augmenting the computational time. These considerations underline the difficulty of defining an appropriate convergence criteria in multiobjective optimization.

The \mathbf{x} in Figure 11 shows the mean values of the two objective functions for each of the Pareto set analyzed before. It is worth noting that the mean values are all within a range of 5%. Their values also show that, as already pointed out, the left branch of the Pareto front is more densely sampled than the right one. The \square and \bullet describe a typical behavior of the algorithm when the constant value $w = 0.4$ is employed for the inertia. In these cases the algorithm tend to locally converge to one of the two branches of the Pareto set, as clearly enlighten in Figure 12.

In Figure 13 the \mathbf{G}_{best} list after 100 iterations of one of the 30 simulations performed is plotted. The Pareto front confirms the considerations reported in Section 3: the volumetric efficiency oriented solutions (bottom right) are compact capsules with higher value of TPS mass; as opposite the TPS oriented solutions tend to have high base radius and to be very short.

Table 2 summarizes the numerical data of the five solutions highlighted in the previous figure. All the solutions tend to the minimum value allowed for the lift-to-drag ratio in order to decelerate the capsule at higher altitudes, thus reducing the TPS mass ratio. Soln 2 to Soln 5 are characterized by almost the same value of the front cone half-angle which allows to consider large nose radii. Soln 1 belongs to a different class of vehicles: the front cone half-angle is the lowest allowed, and the forebody is longer than the aftbody. The difference between these two classes of vehicles is highlighted also by the different sign of the lift-to-drag ratio: Soln 1 is the only shape that produces negative C_L for negative angles of attack. Eventually, note that TPS oriented solutions have higher values of minimum altitude, shallower entry angles, and lower ballistic coefficient.

The maximum of TPS% is 13.30, which results in 126 kg of TPS mass in the worse case solution. In order to establish the aerocapture effectiveness, the TPS mass must be compared with the propellant required for the circularization without employing aerocapture. This value is computed in a 2-body approximation and the spacecraft is assumed to

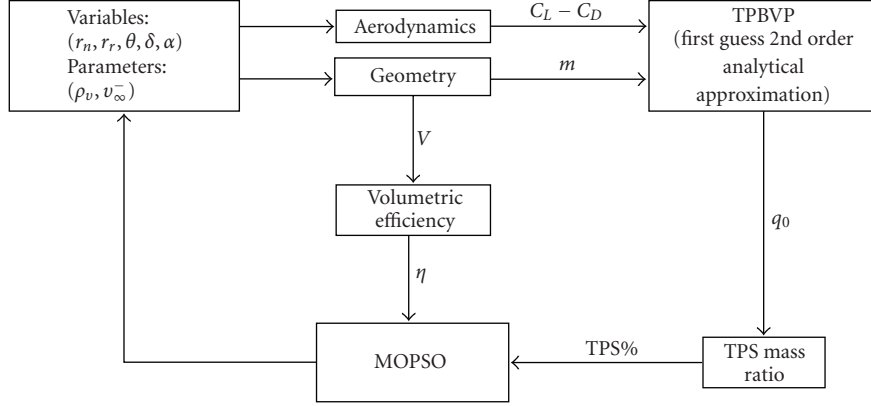


FIGURE 9: Aerocapture optimization scheme.

TABLE 2: Numerical results for five solutions belonging to the Pareto optimal set.

Parameter		Soln 1	Soln 2	Soln 3	Soln 4	Soln 5
TPS%	—	13.28	9	7.9	7.5	6.1
η	m^{-2}	0.46	0.55	0.63	0.68	0.89
α	deg	-29.45	-21.13	-19.3	-20.3	-19.27
σ	deg	57.4	116.9	117.2	115.8	115
C_L/C_D	—	-0.31	0.32	0.30	0.31	0.30
$m/(SC_D)$	kg/m^2	299.72	120.26	86.13	77.11	45.02
h_{\min}	km	36.5	43.9	46.7	47.7	52.3
γ_e^-	deg	-9.08	-8.50	-8.25	-8.19	-7.73
r_b	m	1.16	1.37	1.59	1.69	2.19
r_n	m	0.73	1.22	1.42	1.52	1.94
r_r	m	0.58	0.47	0.45	0.48	0.82
θ	deg	21	68.51	70	69.64	70
δ	deg	41	56.59	40	42.07	5.2

switch on the thrusters at the hyperbola pericenter, located at 200 km of altitude. The Δv required to circularize the orbit is given by

$$\Delta v = \sqrt{\frac{\mu}{r_a} + v_{\infty}^{-2}} - \sqrt{\frac{\mu}{r_a}} \quad (23)$$

and the propellant fraction by rocket equation

$$\frac{m_p}{m} = 1 - e^{-(\Delta v/I_{sp}g_0)}, \quad (24)$$

in which I_{sp} is the thruster specific impulse, and $g_0 = 9.81 \text{ m/s}^2$ represents the Earth gravitational acceleration at sea level. For a value of $I_{sp} = 400 \text{ s}$ it results $m_p/m = 0.594$, which means that more than the 59% of the spacecraft should be propellant, largely greater than the 13.30% of TPS. Therefore the aerocapture represents an effective means to reduce the propellant compared to a classical orbital circularization, thus significantly increasing the mass specifically devoted to the payload. In the following section, the refinement of the Soln 2 and Soln 3 is addressed, as they show a good compromise between volumetric efficiency and TPS mass ratio.

5. TRAJECTORY REFINEMENT

The dynamical model applied for the solution of the TPBVP considers the evolution of the velocity, the altitude, and the flight path angle only, and terms of order $\Delta r/r_e$ are neglected.

In order to address the problem of achieving the 3D target orbit the complete dynamical model (3) is considered. The constant bank angle approximation is lifted and an optimal control problem is formulated to optimize the bank profile. In the trajectory refinement the vehicle's shape is fixed and the constant angle of attack strategy is retained, taking advantage of the values computed in the coupled trajectory-shape optimization. Thus, all the variables considered in the former optimization are fixed parameters. The state and control vectors are $\mathbf{x} = (r, \theta, \varphi, v, \gamma, \psi)^T$ and $\mathbf{u} = \sigma$, respectively. The initial conditions are expressed by

$$\begin{aligned} r_e^- &= r_e, \\ \mathbf{v}_{\infty}^-(\mathbf{x}_e^-) &= \mathbf{v}_{\infty}^-. \end{aligned} \quad (25)$$

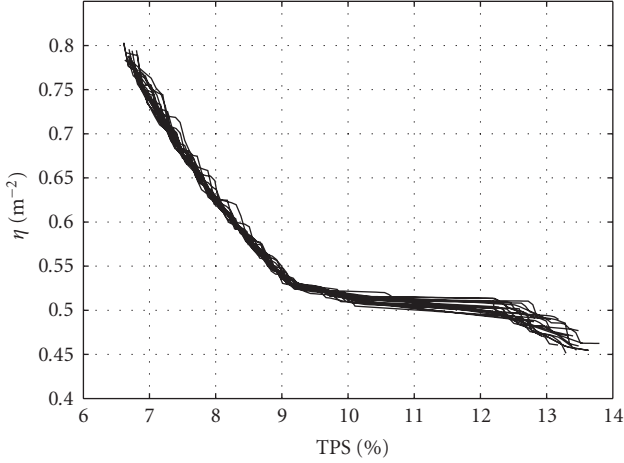


FIGURE 10: Cubic spline interpolated Pareto optimal sets.

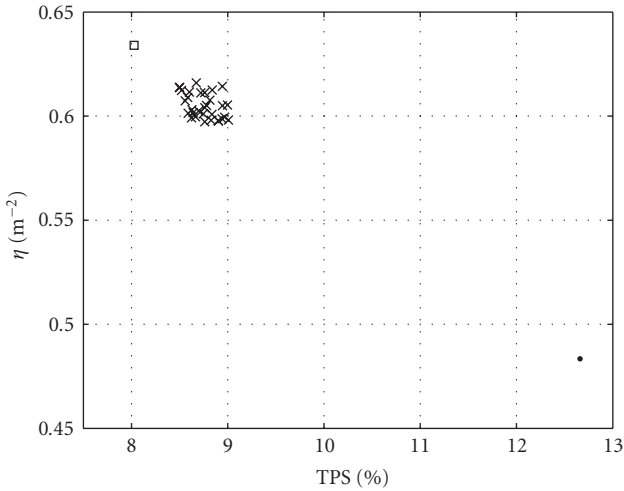


FIGURE 11: Mean values of the Pareto optimal solutions.

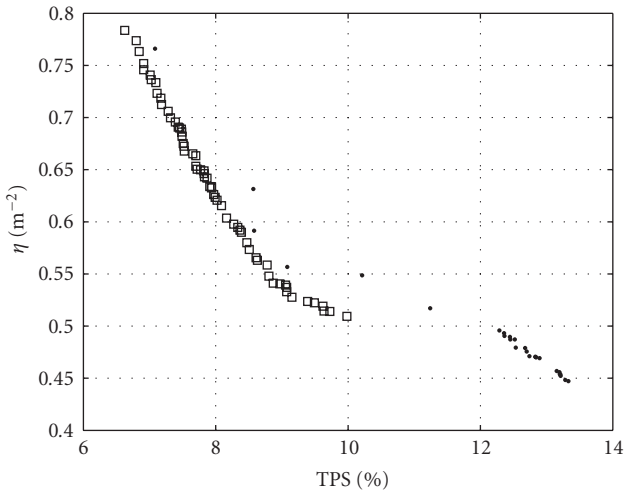
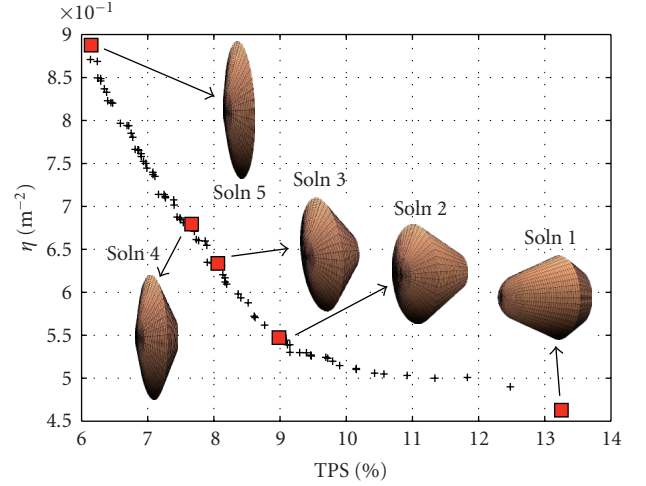
FIGURE 12: Two examples of local convergences ($w = 0.4$).

FIGURE 13: Aerocapture Pareto optimal solutions.

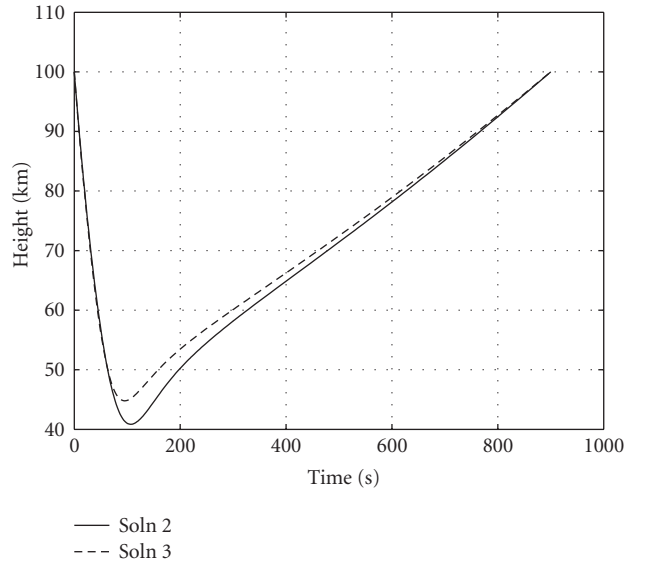


FIGURE 14: Soln 2 and Soln 3 refined solution: height profile.

The scalar constraint assures that the maneuver begins at the planet atmosphere interface. The vectorial constraint states that the incoming velocity at the planet sphere of influence corresponding to the initial state \mathbf{x}_e^- , that is, $\mathbf{v}_\infty^-(\mathbf{x}_e^-)$, must be equal to the spacecraft incoming velocity \mathbf{v}_∞^- , imposed by the heliocentric trajectory analysis. The optimizer exploits the two degrees of freedom on the initial state to choose the proper entry plane in the Martian atmosphere. The following three scalar constraints are enforced on the final position:

$$\begin{aligned} r_e^+ &= r_e, \\ a \sin\left(\frac{\Gamma_{e,z}^+}{\Gamma_e^+}\right) &= \frac{\pi}{2}, \end{aligned} \quad (26)$$

$$-\frac{\mu}{v_e^{+2} - (2\mu/r_e^+)} \left(1 + \left\| \frac{\mathbf{v}_e^+ \times \boldsymbol{\Gamma}_e^+}{\mu} - \frac{\mathbf{r}_e^+}{r_e^+} \right\|^2\right) = r_a$$

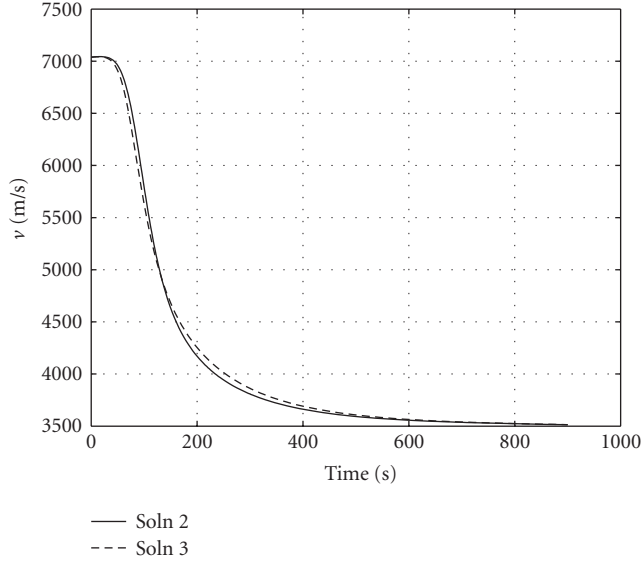


FIGURE 15: Soln 2 and Soln 3 refined solution: velocity magnitude.

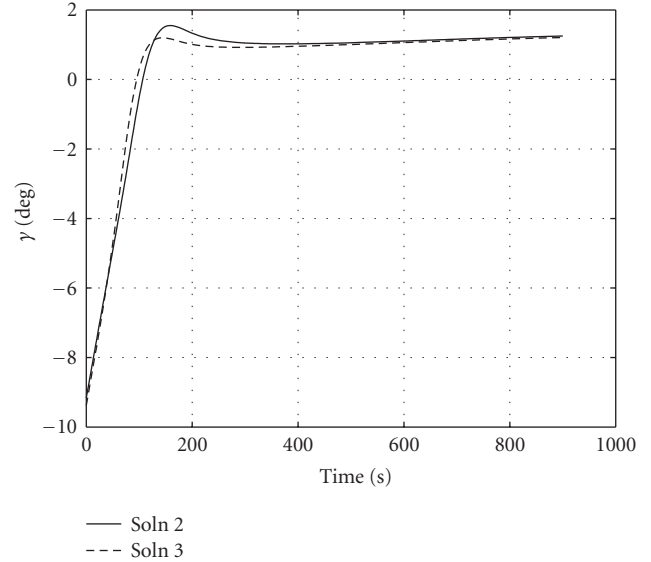


FIGURE 16: Soln 2 and Soln 3 refined solution: flight path angle.

The first constraint assures that the trajectory ends at the atmospheric boundary, whereas the remaining two guarantee the exit trajectory to be polar and with an apogee lying on the target orbit. If the additional constraint $\gamma_e^+ = 0$ is considered, thus achieving the theoretical minimum $\Delta v = 24.4$ m/s as explained in Section 3, the local optimizer fails to converge. More specifically, the tight relative tolerance of 10^{-8} on the constraints satisfaction is violated. This problem is avoided if the constraint on the final flight path angle is dropped and the Δv minimization is addressed. Thus the objective function is

$$J = \Delta v = \sqrt{\frac{\mu}{r_a}} - \sqrt{v_e^{+2} - 2\mu\left(\frac{1}{r_e^+} - \frac{1}{r_a}\right)}, \quad (27)$$

in which the first term represents the target orbit velocity and the second one the vehicle's velocity at the apogee.

For each shape the TPS% is bounded by the value of the coupled shape-trajectory optimization. In order to evaluate the constraint, the stagnation heat load is added to the state vector and it is integrated along with the dynamics. The trajectory is split into four multiple shooting intervals, and the integration is performed adopting a 8th order fixed-step Runge-Kutta scheme with absolute and relative tolerances of 10^{-8} . The optimal solution is found using a sequential quadratic programming (SQP) optimizer.

The results obtained for the Soln 2 and Soln 3 are shown in Figures 14–17. For both the solutions the value of the minimum altitude is slightly lower than the one found in the previous section due to a steeper entry flight path angle. The optimizer completely changes the bank control law; the bank modulation is exploited to minimize the Δv and mainly to match the target orbital plane. Note that the maximum value of the aerodynamic forces on the trajectory is reached during the deepest phase in the atmosphere, when the bank angle is not far from the value found in the coupled shape-trajectory optimization. Furthermore, if most of the points describing

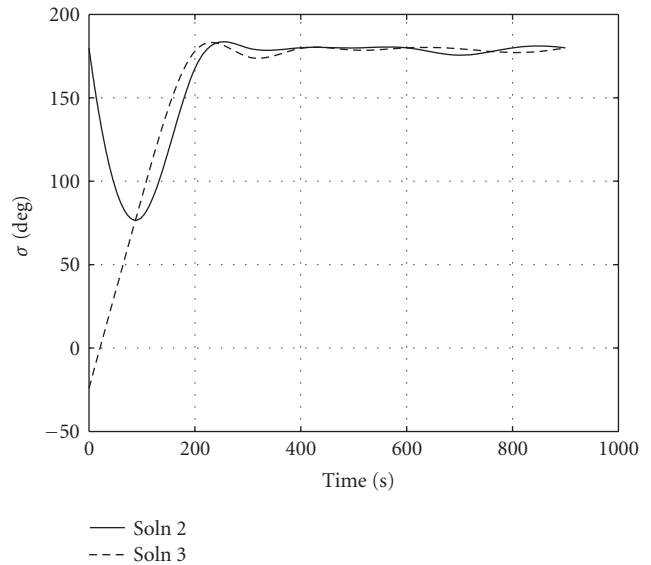


FIGURE 17: Soln 2 and Soln 3 refined solution: bank profile.

the optimal bank angle spline are substituted by the constant bank angle value computed in the shape-trajectory optimization, only a slight change in the trajectory is obtained. Moreover the trajectory refinement has a high convergence rate when the constant bank angle law is used as first guess solution. These considerations prove that the assumptions adopted in Section 4 deliver sufficiently accurate results.

The Δv is 39.22 m/s for Soln 2 and 38.25 m/s for Soln 3, close to the theoretical minimum of 24.4 m/s, and slightly lower than the 52.6 m/s constraint of the shape-trajectory optimization. Furthermore, the TPS mass ratio is lower compared to the one found in the shape-trajectory optimization for both of the solutions. This result is a consequence of the shorter permanence of the vehicles in the lower layers of Mars

TABLE 3: Aerocapture trajectory refinement: numerical results.

	h_{\min} [km]	γ_e^- [deg]	TPS%	Δv [m/s]
Soln 2	40.85	-9.16	7.98	39.22
Soln 3	44.8	-9.38	7.05	38.25

atmosphere. Note that, although the trajectory refinement changes the value of the TPS mass, the trend highlighted in the previous section still holds, that is, a higher ballistic vehicle requires a higher TPS mass. The main results of the trajectory refinement are summarized in Table 3.

6. CONCLUSIONS

The use of an MOPSO for the optimization of an aerocapture maneuver at Mars from a multidisciplinary-multiobjective standpoint is presented. More specifically, the interaction among vehicle's shape, trajectory control, and TPS design is taken into account in the preliminary design of the maneuver. The aerocapture multiobjective optimization emphasizes the conflict between volumetric efficiency maximization and thermal protection system mass ratio minimization. Solutions that show a compromise between the two objective goals have shapes similar to those adopted in previous landing missions to Mars. Aerocapture maneuver is demonstrated to be a valid means for lowering the propellant required to accomplish interplanetary missions if compared to classical circularization maneuvers. The models adopted are suitable for Phase-A studies of future aerocapture missions, and the proposed method properly matches the requirements of concurrent engineering, which is nowadays the leading approach in aerospace field. The MOPSO, although of simple implementation, effectively compute the Pareto optimal solution set of a complex engineering problem using low number of function evaluations. The advantage of having a set of Pareto optimal solutions is of vital importance in aerospace field, where most of the design processes are characterized by the interaction of several subsystems and disciplines, and it is often impossible to identify a single performance index. Based on these considerations, in the authors belief, MOPSO could be successfully applied to a broad set of aerospace engineering problems, especially in system design and trajectory optimization fields.

REFERENCES

- [1] M. I. Cruz, "The aerocapture vehicle mission design concept," in *Proceedings of the AIAA Joint Propulsion Conference*, 1979, AIAA paper 79-0893.
- [2] M. Bello Mora and G. Dutruel-Lecohier, "Reentry and aeroassisted transfer trajectory optimal control: the gradient restoration algorithm," in *Proceedings of the 3rd International Conference on Space Guidance, Navigation, and Control Systems (ES-TEC '96)*, pp. 95–101, Noordwijk, The Netherlands, November 1996.
- [3] K. D. Mease, "Optimization of aeroassisted orbit transfer: current status," *Journal of the Astronautical Sciences*, vol. 36, no. 1 part 2, pp. 7–33, 1988.
- [4] N. X. Vinh, W. R. Johnson, and J. M. Longusky, "Mars

- aerocapture using bank modulation," in *Proceedings of the AIAA/AAS Astrodynamics Specialist Conference*, Denver, Colo, USA, August 2000, collection of technical papers.
- [5] E. Sigal and M. Guelman, "Optimal aerocapture with minimum total heat load," in *Proceedings of the 52nd International Astronautical Congress*, Toulouse, France, October 2001.
- [6] D. Vaughan, H. C. Miller, B. Griffin, B. F. James, and M. M. Munk, "A comparative study of aerocapture missions with a Mars destination," in *Proceedings of the 41st AIAA/ASME/SAE/ASEE Joint Propulsion Conference and Exhibit*, Tucson, Ariz, USA, July 2005.
- [7] S. A. Whitmore, D. W. Banks, B. M. Andersen, and P. R. Jolley, "Direct—entry, aerobraking, and lifting aerocapture for human-rated lunar return vehicles," in *Proceedings of the 44th AIAA Aerospace Sciences Meeting and Exhibit*, Reno, Nev, USA, January 2006.
- [8] R. D. Braun and R. W. Powell, "Aerodynamic requirements of a manned aerobraking transfer vehicle," in *Proceedings of the AIAA Atmospheric Flight Mechanics Conference*, Portland, Ore, USA, August 1990.
- [9] K. J. Sudmeijer and E. Mooij, "Shape optimization for small experimental re-entry module," in *Proceedings of the 11th AIAA International Space Planes and Hypersonic Systems and Technologies Conference*, Orleans, France, September-October 2002.
- [10] R. Armellin, M. Lavagna, R. P. Starkey, and M. J. Lewis, "Aerogravity-assist maneuvers: coupled trajectory and vehicle shape optimization," *Journal of Spacecraft and Rockets*, vol. 44, no. 5, pp. 1051–1059, 2007.
- [11] R. C. Eberhart and J. Kennedy, "A new optimizer using particle swarm theory," in *Proceedings of the 6th International Symposium on Micro Machine and Human Science*, pp. 39–43, Nagoya, Japan, October 1995.
- [12] J. Kennedy and R. C. Eberhart, "Particle swarm optimization," in *Proceedings of IEEE International Conference on Neural Networks (ICNN '95)*, vol. vol. 4, pp. 1942–1948, Perth, Western Australia, November-December 1995.
- [13] R. Poli, J. Kennedy, and T. Blackwell, "Particle swarm optimization: an overview," *Swarm Intelligence Journal*, vol. 1, no. 1, pp. 33–57, 2007.
- [14] X. Hu and R. Eberhart, "Multiobjective optimization using dynamic neighborhood particle swarm optimization," in *Proceedings of the Congress on Evolutionary Computation (CEC '02)*, vol. vol. 2, pp. 1677–1681, Honolulu, Hawaii, USA, May 2002.
- [15] K. E. Parsopoulos and M. N. Vrahatis, "Particle swarm optimization method in multiobjective problems," in *Proceedings of ACM Symposium on Applied Computing (SAC '02)*, pp. 603–607, Madrid, Spain, March 2002.
- [16] T. Ray and K. M. Liew, "A swarm metaphor for multiobjective design optimization," *Engineering Optimization*, vol. 34, no. 2, pp. 141–153, 2002.
- [17] C. A. Coello Coello and M. S. Lechuga, "MOPSO: a proposal for multiple objective particle swarm optimization," in *Proceedings of the Congress on Evolutionary Computation (CEC '02)*, pp. 1051–1056, Honolulu, Hawaii, USA, May 2002.
- [18] C. A. Coello Coello, G. T. Pulido, and M. S. Lechuga, "Handling multiple objectives with particle swarm optimization," *IEEE Transactions on Evolutionary Computation*, vol. 8, no. 3, pp. 256–279, 2004.
- [19] J. D. Anderson, *Hypersonic and High Temperature Gas Dynamics*, McGraw-Hill, New York, NY, USA, 1989.
- [20] B. J. McBride and S. Gordon, "Computer program for calculation of complex chemical equilibrium compositions and

- applications II. User's manual and program description," Tech. Rep. E-8017-1, NASA Lewis Research Center, Cleveland, Ohio, USA, 1996.
- [21] K. A. Edquist, "Computations of viking lander capsule hypersonic aerodynamics with comparisons to ground and flight data," in *Proceedings of AIAA Atmospheric Flight Mechanics Conference and Exhibit*, Keystone, Colo, USA, August 2006.
- [22] B. Laub and E. Venkatapathy, "Thermal protection system technology and facility needs for demanding future planetary missions," in *Proceedings of International Workshop on Planetary Probe Atmospheric Entry and Descent Trajectory Analysis and Science*, Lisbon, Portugal, October 2003.
- [23] M. Tauber and J. Bowles, "The use of atmospheric braking during mars missions," in *Proceedings of the 4th AIAA Thermophysics Conference*, Buffalo, NY, USA, June 1989.
- [24] R. H. Battin, *An Introduction to the Mathematics and Methods of Astrodynamics*, Aiaa Education Series, Reston, Va, USA, 1999.
- [25] L. Quartapelle and S. Rebay, "Numerical solution of two-point boundary value problems," *Journal of Computational Physics*, vol. 86, no. 2, pp. 314–354, 1990.
- [26] L. Quartapelle and A. Scandroglio, "Solution of the Falkner-Skan Equation to Determine Reverse Flow," DIA-SR 03-05, 2003.
- [27] R. Armellin and F. Topputo, "A sixth-order accurate scheme for solving two-point boundary value problems in astrodynamics," *Celestial Mechanics and Dynamical Astronomy*, vol. 96, no. 3-4, pp. 289–309, 2006.
- [28] J. Kennedy and R. C. Russel, *Swarm Intelligence*, Morgan Kaufmann Publishers, San Fransisco, Calif, USA, 2001.
- [29] K. Deb, "Evolutionary algorithms for multi-criterion optimization in engineering design," in *Evolutionary Algorithms in Engineering and Computer Science*, pp. 135–161, John Wiley & Sons, Chichester, UK, 1999.
- [30] G. Coath and S. K. Halgamuge, "A comparison of constraint-handling methods for the application of particle swarm optimization to constrained nonlinear optimization problems," in *Proceedings of the Congress on Evolutionary Computation (CEC '03)*, vol. vol. 4, pp. 2419–2435, Canberra, Australia, December 2003.